CSIRO PUBLISHING

International Journal of Wildland Fire **2016**, *25*, 76–89
http://dx.doi.org/10.1071/WF14154

Observations of energy transport and rate of spreads from low-intensity fires in longleaf pine habitat – RxCADRE 2012

B. Butler[A,D], *C. Teske*[B], *D. Jimenez*[A], *J. O'Brien*[C], *P. Sopko*[A], *C. Wold*[A], *M. Vosburgh*[A], *B. Hornsby*[C] *and E. Loudermilk*[C]

[A]USDA Forest Service, Rocky Mountain Research Station, Fire Sciences Laboratory, Missoula, MT 59801, USA.
[B]Center for Landscape Fire Analysis, University of Montana, Missoula, MT 59812, USA.
[C]USDA Forest Service, Southern Research Station, Athens Fire Laboratory, Athens, GA 30602, USA.
[D]Corresponding author. Email: bwbutler@fs.fed.us

Abstract. Wildland fire rate of spread (ROS) and intensity are determined by the mode and magnitude of energy transport from the flames to the unburned fuels. Measurements of radiant and convective heating and cooling from experimental fires are reported here. Sensors were located nominally 0.5 m above ground level. Flame heights varied from 0.3 to 1.8 m and flaming zone depth varied from 0.3 to 3.0 m. Fire ROS derived from observations of fire transit time between sensors was 0.10 to 0.48 m s^{-1}. ROS derived from ocular estimates reached 0.51 m s^{-1} for heading fire and 0.25 m s^{-1} for backing fire. Measurements of peak radiant and total energy incident on the sensors during flame presence reached 18.8 and 36.7 kW m^{-2} respectively. Peak air temperatures reached 1159°C. Calculated fire radiative energy varied from 7 to 162 kJ m^{-2} and fire total energy varied from 3 to 261 kJ m^{-2}. Measurements of flame emissive power peaked at 95 kW m^{-2}. Average horizontal air flow in the direction of flame spread immediately before, during, and shortly after the flame arrival reached 8.8 m s^{-1}, with reverse drafts of 1.5 m s^{-1}; vertical velocities varied from 9.9 m s^{-1} upward flow to 4.5 m s^{-1} downward flow. The observations from these fires contribute to the overall understanding of energy transport in wildland fires.

Additional keywords: energy transport, field measurements, fire behaviour, fire modelling.

Received 4 September 2014, accepted 16 July 2015, published online 15 December 2015

Introduction

Energy transfer drives wildland fire ignition, rate of spread (ROS) and intensity (Anderson 1969; Yedinak *et al.* 2006; Anderson 2010). Quantification of energy transport in wildland fires, particularly the variability in space and time and the proportion released through radiant and convective heating modes, is a critical yet poorly documented element of wildland fire science (Frankman *et al.* 2013*a*). Although radiative energy transport has received the bulk of the interest in wildland fire research (Albini 1985; Albini 1986), recent studies have focussed on understanding the role of both radiative and convective energy transport to wildland fire ignition and spread (Morandini and Silvani 2010; Yedinak *et al.* 2010). For example, the radiometric properties of the energy emitted from wildland flames has been of particular interest (Parent *et al.* 2010), as has analysis of heat flux measurement uncertainty in flames (Bryant *et al.* 2003; Pitts *et al.* 2006). However, understanding of the properties of energy transfer in wildland flames is still limited (Sacadura 2005; Viskanta 2008; Finney *et al.* 2010), likely due to complex logistics associated with sensor deployment, the high-temperature environment, and the natural variability in fire intensity over time and space. When considering relationships between energy transport in wildland flames and particle ignition it is unclear how woody particles respond to temporal fluctuations in the heating source. An analytical solution to small particle heating (Frankman 2009) demonstrates that particle time to ignition is related to both the periodicity and magnitude of the heating source. It also shows that these two factors are directly correlated (i.e. lower frequency signals result in ignition at lower magnitudes). Thus the temporal characteristics of the heating regime are relevant to additional understanding of wildland fire. To understand and accurately predict the behaviour of forest fires (Albini 1996), model fire emissions (Wooster *et al.* 2005; Freeborn *et al.* 2008; Urbanski *et al.* 2008), and improve public and wildland firefighter safety (Butler and Cohen 1998; Butler 2014), it is critical to understand how energy is released from burning wildland fires.

Studies have explored energy transport in wildland fires for a century, but it is only in the past decade that significant progress has been made on this topic. Radiative heating magnitudes as high as 300 kW m^{-2} have been measured in wildland fires (Butler 2003; Butler *et al.* 2004; Frankman *et al.* 2013*a*). Only a limited number of measurements of convective energy transport

Journal compilation © IAWF 2016

have been reported. Anderson *et al.* (2010) measured horizontal air flow near the fuel bed surface and found that immediately before flame arrival there was an in-draft (opposite the wind pushing the flames) followed by a sharp spike in flow in the direction of flame spread as the flames burned over the sensor. This pattern was also observed by Clements *et al.* (2007) and can be correlated with the measurements of convective energy transport reported here. In general, the data measured in these studies indicate that convective energy transport immediately before and after arrival of the flame alternates between heating and cooling with peak magnitudes of 22–140 kW m^{-2} (under ideal flame spread conditions). The convective energy transport is characterised by rapid fluctuation between positive and negative convection values owing to alternating packets of cool air intermingled with hot combustion products.

There is still much that is not understood about energy transport in fires burning natural fuels. Some current questions are (1) how does the relative contribution of radiant and convective heating vary with vegetation and burning environment; (2) what are the temporal characteristics of each; (3) does the contribution of each vary through the burning period; (4) how does each contribute to ignition and fire spread; and (5) does fire energy release relate to emissions production and if so in what way?

Recognising the need for additional understanding of energy transport in fires, the RxCADRE project was initiated to collect a comprehensive set of data that address these and other critical research needs (Ottmar *et al.* 2015). This document focuses on ground-based video cameras and sensors that characterise energy transport at or within 0.5 m of the ground surface. Here we report flame geometry, ROS, energy measurements and fire type (i.e. heading, flanking or backing). Specifically, time-resolved convective and radiative heat flux, air temperature, vertical and horizontal velocity, and flame emissive power from fires burning in two vegetation types are discussed. Calculated values include flame radiative energy and flame convective energy. The measurements collected as part of this study can be used to develop a new understanding of the relative contribution of radiative and convective heating to overall energy transport in and around wildland fires under a variety of conditions, and inform the characterisation of emissions from wildland fires.

Methods

Experimental location

Burns were conducted during the month of November 2012, on Eglin Air Force Base in North-west Florida (USA). Approximate location of the burn plots was 30°32′35″N, 86°44′33″W, at an elevation 46 m above sea level. Nine plots were burned: six plots measured 100 × 200 m in size and were selected for their relatively uniform grass vegetation and absence of overstorey vegetation; two large grass plots and one large plot with a conifer overstorey were also burned. The plots were consistently flat, and exposed to a 300–600-m upwind fetch with little or no overstorey vegetation. Data were collected in all burn plots; here we report measurements from the two plots that burned with what we observed to be the most consistent, uniform flame front (i.e. plots S5 and L2G). Fuel loading, consumption and moisture content as well as ambient conditions at the time of the burn are presented in Table 1. Additional details on fuel parameters are presented in Ottmar *et al.* (2015). The small grass plots were ignited with a line fire initiated by hand-held drip torches near the upwind edge of the plot. The large burn plots were ignited following a strip head fire method using drip torches mounted on an all-terrain vehicle (ATV) moving across the plots over strips of nominal 10–20 m width.

Sensors

A system consisting of temperature, air flow and energy sensors for quantifying energy and mass transport in wildland fires was used to characterise the effect of fuel treatment on fire spread and intensity (Butler and Jimenez 2009). The system consists of two types of enclosure: a sensor/datalogger combination mounted in an aluminium housing that allows *in situ* characterisation of convective/radiant energy transport in wildland fires; and a video camera enclosure. The first type of housing, termed the fire behaviour package (FBP), measures 27 × 15 × 18 cm and weighs ~5.3 kg. It contains rechargeable batteries, a programmable datalogger, a Medtherm© Dual Heat Flux sensor (Model 64–20T) of the Schmidt–Boelter style that provides incident total and radiant energy flux, a type K fine wire thermocouple (nominally 0.025-mm diameter wire), a custom designed narrow angle radiometer (NAR) (Butler 1993), and two pressure-based flow sensors – one oriented to sense horizontal flow and one to sense vertical flow (McCaffrey and Heskestad 1976). The sensors were calibrated before deployment as described elsewhere (Butler and Jimenez 2009). The fine wire thermocouple has a response time of ~0.01 s (Omega Engineering n.d.) and was used to sense flame presence and flame residence time. Convective heat flux at the sensor face can be estimated from the total and radiant sensors with some correction for transmission through the radiometer window (Frankman *et al.* 2013*a*). Integration of the heat flux time histories provides a measure of fire total, radiative and convective energy per unit area as a function of heating time. A recent study has shown that, for 5-Hz sampling rates, the difference between measured and actual peak radiative heating

Table 1. Fuel and weather conditions (see Ottmar *et al.* 2015)

Burn unit	Pre-fire fuel load (Mg ha^{-1}) herb/shrub/fine wood/litter	Consumption (%) herb/shrub/fine wood/litter	Fuel moisture (% dry mass basis) herb/shrub/litter	Air temperature (°C)	Relative humidity (%)	Ambient wind speed – direction (m s^{-1} – °)
S5	1.70/0.54/0.02/0.55	91/29/64/85	105/173/9	24.5	24.1	2.9–250
L2G HIP 1	1.94/0.47/0.00/0.37	95/80/–/87	82/131/8			
L2G HIP 2	2.01/0.01/0.22/0.73	92/74/75/100		22.2	41.0	1.3–0
L2G HIP 3	1.74/3.03/0.09/1.01	94/88/–/99				

rates can be as great as 24% and on the order of 80% for 1-Hz sampling rates (Frankman *et al.* 2013*b*). The study also demonstrated that heating rates averaged over a 2-s period were insensitive to sampling rate across all ranges explored. In an effort to reduce measurement error for this study all sensor data were recorded at 10 Hz.

The second type of housing is a fireproof enclosure containing a video camera (Jimenez *et al.* 2007). The camera enclosure system weighs ~1.8 kg, measures 10 × 18 cm × 19 cm, and is constructed of 1.6-mm aluminium. The camera's enclosure system double lens configuration consists of high-temperature Pyrex© glass and a second lens with a multi-layer dielectric coating that reflects infrared radiation (heat) while allowing visible light to pass through. The preferred video cameras were GoPro© Hero-3 cameras.

Each FBP typically is coupled with a video camera system for simultaneous recording of video and *in situ* measurements, allowing researchers to better evaluate fire behaviour measurements relative to flame size and local ROS. Visual analysis of the video images provides one method for measuring flame height, flame length, flame depth, flame angle and fire ROS, provided that a calibration object is in the camera's field of view. Both the FBP and camera enclosures are designed to be mounted on tripods. Once mounted on tripods, the FBP and cameras are powered up, and a single layer of 2.5-cm thick ceramic blanket and fibreglass reinforced aluminium foil material is wrapped around the box.

FBPs and in-fire video recorders were deployed on burn plot S5 as shown in Fig. 1. The FBPs were located roughly along a transect parallel to the long axis of the burn plot. Sensors and cameras were deployed in burn plot L2G in the same vicinity as highly instrumented plots (HIP) associated with measurements by others (see other articles in this issue). In all cases the FBPs were positioned to sense fire from the expected spread direction based on wind direction, terrain slope and lighting procedures. Typically one camera and one or two FBPs were paired and deployed together. The cameras were oriented to provide images of the fire as it approached and burned over the respective FBPs; that is, cameras 'looked' towards an FBP in an angle perpendicular to expected fire spread. All FBPs were located nominally 0.5 m above the mineral soil; cameras were positioned 0.5–1.0 m above the ground. The cameras and FBPs were oriented to 'look' horizontally in the direction they faced: the FBPs towards the expected fire and the cameras obliquely to the fire spread direction. The thermocouples sensed air temperature nominally 0.5 m above ground level. NARs were included that

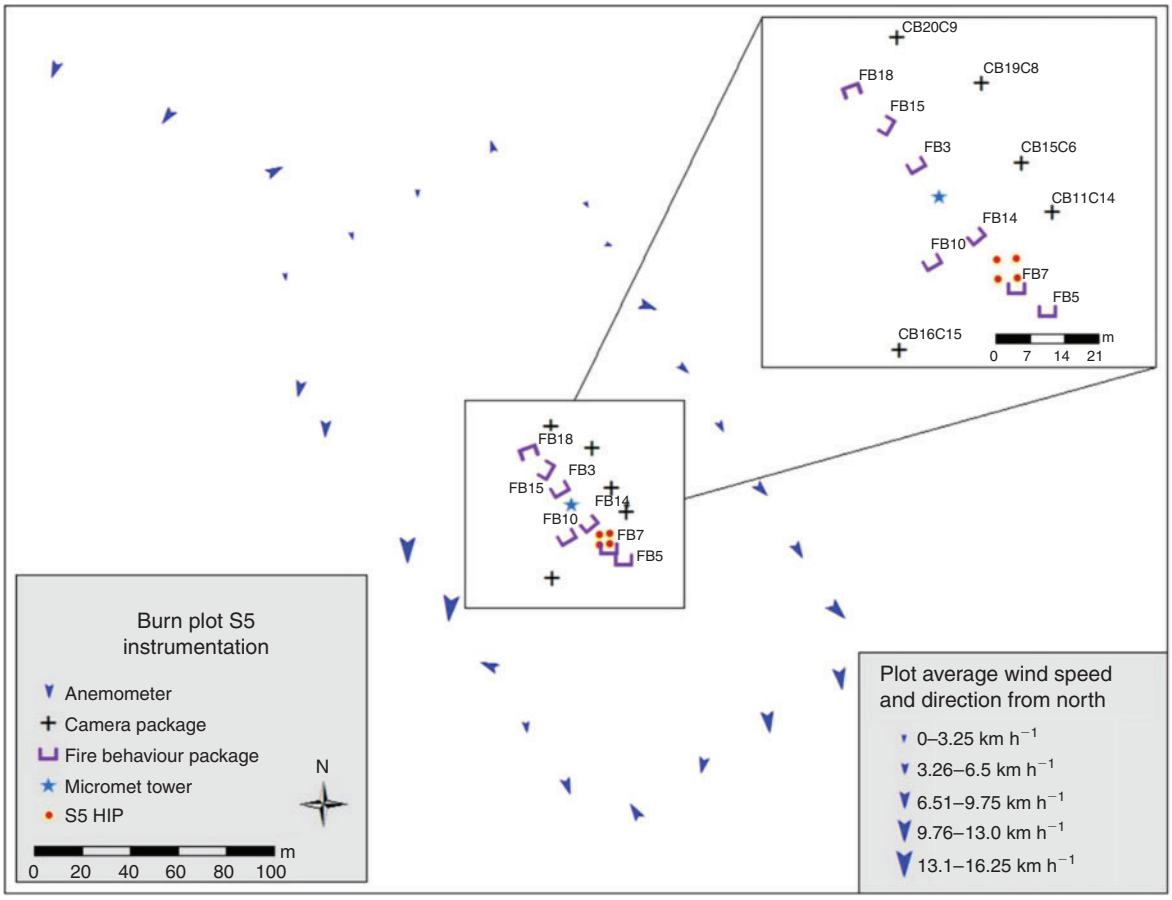

Fig. 1. Sensor layout for burn plot S5. Vectors represent wind speed and direction with the size corresponding to speed and the orientation to direction at 1815 hours GMT. The 60-s average wind speed was 3 m s^{-1} coming from 250°, maximum wind speed was 7.3 m s^{-1}, and minimum was 0.

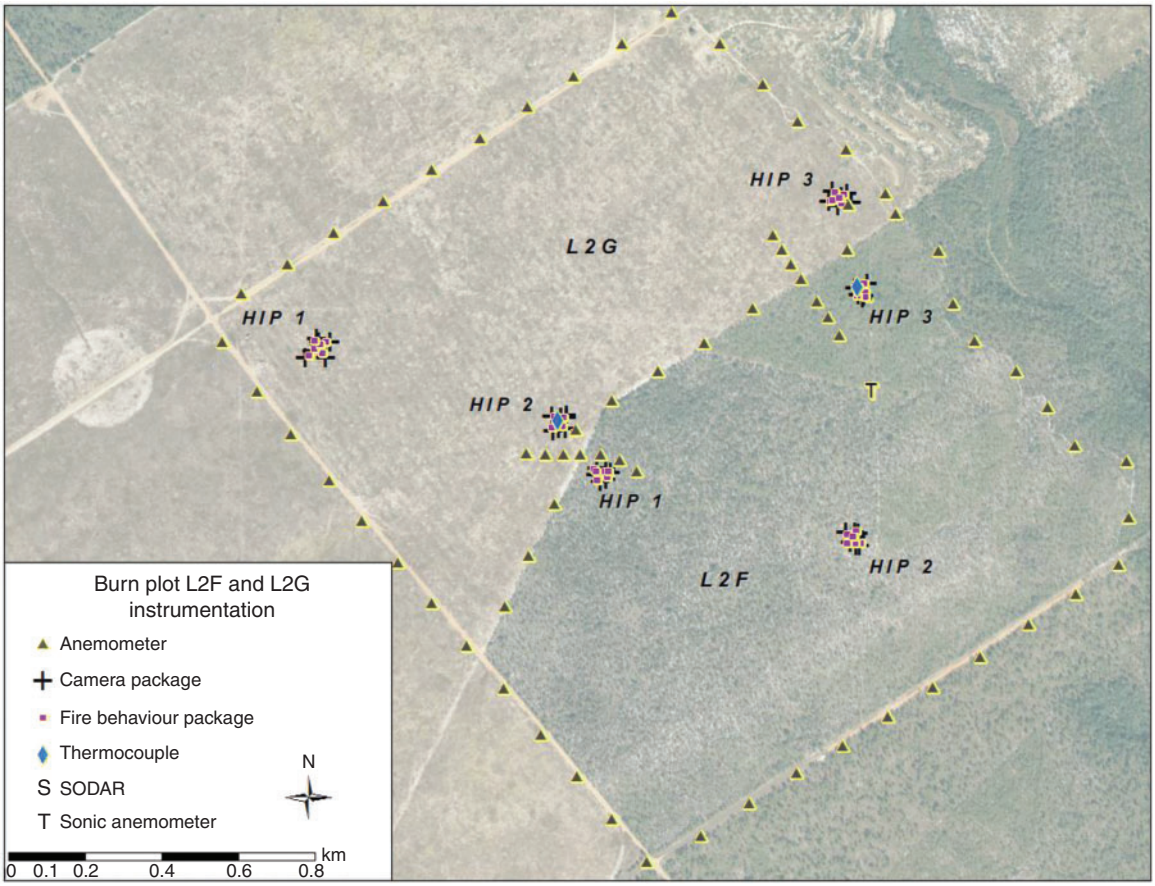

Fig. 2. Sensor layout and general location of burn plots L2G and L2F.

looked horizontally towards the direction faced by the FBP and sensed energy emitted from a nominal 7° field of view.

Flame arrival at the FBP was indicated by a very rapid increase (~3000–5000°C s^{-1}) in temperature to several hundreds of degrees above ambient. This temperature increase was almost always associated with a nearly instantaneous increase in total heat flux at the sensor (10–100 kW m^{-2} s^{-1}). The completion of the flame event was indicated by a rapid decrease in air temperature. In some cases the thermocouple failed, in which case the radiometer data alone were used to gauge the arrival and completion of flaming combustion.

Data analysis

Incident radiant, and total heat flux at the surface of the FBP were evaluated to determine convective energy transport at the sensor face (Frankman *et al.* 2010). Video images were correlated with energy transport measurements to evaluate local flame geometry and ROS. Horizontal and vertical air flow measurements were adjusted for sensor bias. Flame radiative and convective energy were calculated by integrating the respective signals over the period of flaming combustion.

Flame geometry

Flame geometry (i.e. flame height, length, depth, and angle) was determined from visual observation of *in situ* video images. Each measurement represents a minimum of three observations derived from various video images. Due to the low intensity of the fire it was difficult to clearly distinguish fire presence, and thus the measurement uncertainty associated with these data are expected to be high.

Rate of spread

ROS data were estimated using the three different methods. The first method estimates ROS based on ignition time, arrival of flame front at each FBP, and distance between FBPs and ignition line. In other words, it is a spatially averaged ROS based on the overall distance from the ignition line to each successive FBP. For burn plot S5, tower mounted infrared video imagery was used to monitor the progress of the fire front and its arrival at the individual FBPs. The second method estimates ROS based on distance between FBPs and the time difference between flame arrival at each FBP as indicated by the infrared images; the third method is based on visual observations of in-fire video footage. Burn plot S5 was ignited using a line ignition, and the FBPs were arranged generally along a transect oblique to the ignition line (Fig. 1), so all three methods were applied to estimate ROS. For plot L2G, all-terrain vehicle terra torches were used to create a line ignition; however, the FBPs were not arranged as oblique transects (Figs 2, 3), nor was any infrared imagery available that contained successive FBPs in the field of view. Therefore,

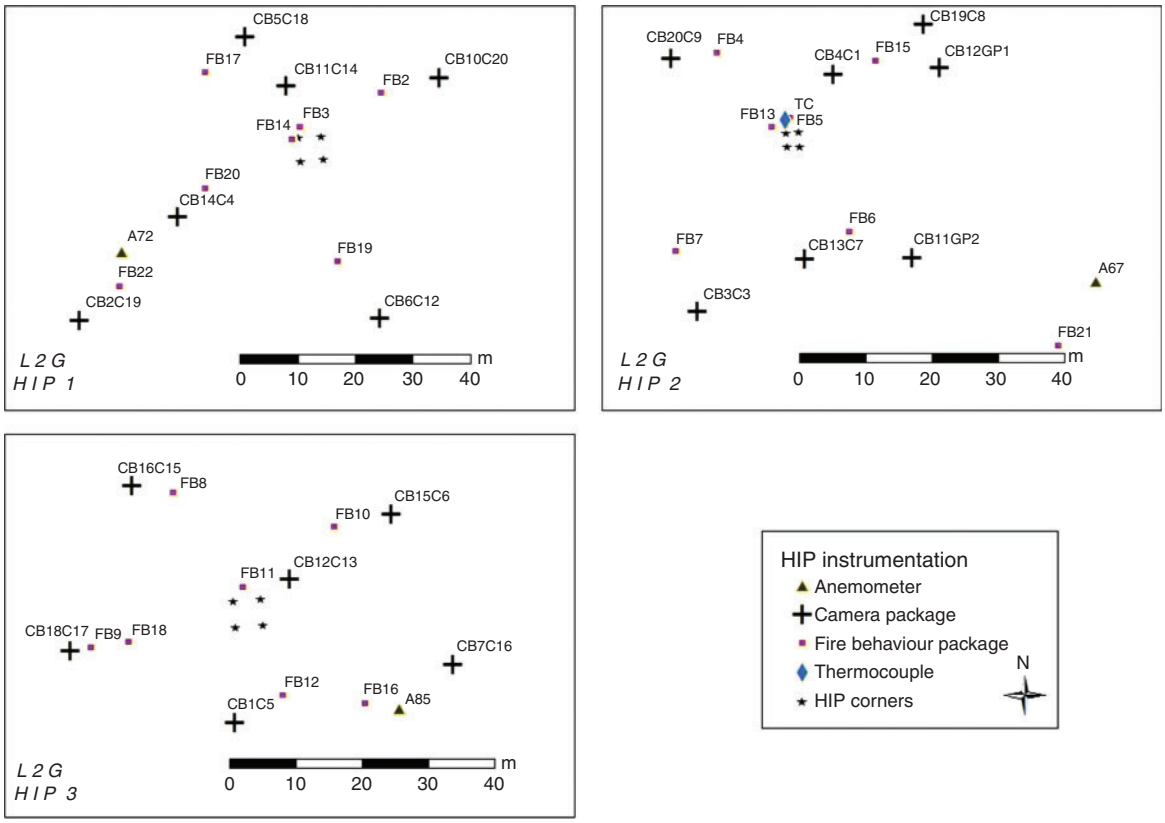

Fig. 3. Highly instrumented plot (HIP) sensor locations for burn plot L2G. Winds were nominally 1.3 m s^{-1} from the north at the time of ignition.

measurement of transit times between FBPs was not possible and consequently only the first and third methods were used to estimate ROS in plot L2G.

For the ROS measurements associated with plot S5, a FLIR© model SC660 infrared camera was located on a boom lift 25.9 m above ground level upwind of the burn plot. The field of view of the oblique imagery covered most of the area of the burn plot and captured the entire fire perimeter from ignition until the fire passed the central instrument cluster and/or reached the downwind control line. The SC660 has a resolution of 640 × 480 pixels, a sensitivity of 0.03°C, a spatial resolution of 1.3 mRad and a thermal accuracy of ±2%. Data were recorded at 1 Hz. Emissivity was set at 0.98 and the air temperature and relative humidity were noted for post-processing. The temperature range during the fires was set to 300–1500°C for collecting active fire infrared data. High-definition digital visual imagery was collected before and during the fire from video cameras located adjacent to the infrared camera. Additional information on this technique and associated data are available in O'Brien *et al.* (2015).

Significant differences between burn plots were explored using analysis of variance (ANOVA) applied to the measurements (i.e. S5, and HIPs 1–3 for burn block L2G) (Table 6).

Results

Characterisation of fire energy transport is dependent on the context for the measurements. For example, remote measurements such as those derived from aircraft- or satellite-based sensors would likely 'see' a different value than ground-based sensors. Similarly the orientation of ground-based sensors likely contributes to the magnitude of energy measured (i.e. oblique views would measure different quantities than nadir views). Total energy released from fires can be many times greater than that measured by ground-based sensors using an oblique view angle (Wooster *et al.* 2005). For the purposes of this investigation, energy emitted generally along or near the ground surface (within 1–5 m) is assumed to be the primary driving factor for fire spread and thus of primary interest to this study.

For this study, fire intensity is characterised by visual observations of flame height, flame length and flame depth; derived ROS values (based on visual observations of video footage, calculations based on infrared images and fire time of arrival in fire behaviour packages); air temperature measurements; total and radiant energy measured incident on the near ground in-fire sensors (FBPs); and derived values for fire radiative energy and fire convective energy.

Fire environment

Air temperature at ignition was 24.5°C for plot S5 and 22.2°C for plot L2G. Relative humidity was 24 and 41% respectively. Wind speed and direction averaged 3 m s^{-1} from 250° for plot S5 at the time of ignition and 1.3 m s^{-1} from the north for plot L2G. Additional discussion of the wind measurements in the context of fire behaviour metrics is presented by Jimenez *et al.* (2014).

Table 2. General observations relating to sensors
FBP, fire behaviour package; ID, identifier

Plot	FBP ID	Associated video camera	FBP/camera comments	Fire comments
S5	18	9	Video failed	Head fire based on data.
	15	8	Temperature sensor failed	Video data suggest nearby flanking fire.
	3	8		Temperature suggest flame presence, video suggests flanking or low-intensity heading fire.
	10	15, 14		Temperature and flux data suggest very low-intensity fire – likely flanking.
	14	6, 14		Temperature and flux data suggest low-intensity, possibly flanking fire.
	7	14, 15		Temperature show fire present, flux data suggest very low-intensity fire – likely flanking.
	5	15		Temperature and flux data clearly show fire was never nearby.
L2G				
HIP 1	22	19		Video shows head and flanking fire at FBP location.
	2	20		Video shows head fire, but FBP not in field of view.
	20	4		Video shows head fire at FBP location.
	3	14		Video shows head fire at FBP location.
	14	14	Temperature sensor failed	Data suggest fire was nearby, but did not directly reach FBP or was of very low intensity.
	19	12		Data suggest fire was nearby, but did not directly reach FBP or was of very low intensity.
	17	18		Data indicate fire arrived at FBP but was low intensity.
HIP 2	21			
	6	7, GP2	Video failed	
	5	1		Video shows head fire at FBP location.
	13	1		Video shows head fire at FBP location.
	15	8, GP1		Video shows head fire at FBP location.
	7	3		Video shows flanking fire at FBP location.
	4	9		Video shows head fire at FBP location.
HIP 3	12	5		Video shows head and flanking fire at FBP location.
	10	6		Video shows spotty fire behaviour at FBP location.
	16	16		Video blurry and FBP not in field of view.
	11	13		Video shows spotty fire behaviour at FBP location.
	8	15		Video shows head and flanking fire at FBP location.
	18	17		Insufficient fuel to carry fire. Burn was patchy.

Fire type

Table 2 presents general observations of fire behaviour that occurred near the FBP sensors and cameras. We attempted to distinguish among heading, flanking and backing fire. Sensor malfunctions are noted. The observations indicate that in burn plot S5 (Fig. 1, 4) the fire arrived at the two sensors nearest the ignition line as a head fire. Subsequent sensors and cameras recorded lower intensities and suggested that the fire front was less organised and spread in several directions. Most of these sensors indicate lower energy release, ROS and flame size, which all suggest lower fire intensity at these locations.

The second burn plot (L2G) (see Figs 2, 3, 4) was much larger than S5. For this burn the sensors were grouped around three individual HIPs. Although the plot was selected for the uniformity of vegetation type, loading and distribution, there remained significant spatial variability in these values. The variability was indicated in the observations of fire spread and intensity. For example, in L2G HIP 1, head fire was indicated for the four sensors nearest the ignition line but flanking fire for the remaining three sensors. Observations in L2G HIP 2 suggest lower-intensity fire at the FBP closest to the ignition line but generally head fire at all other sensors, whereas L2G HIP 3 seems to have burned with lower intensity and more sporadic fire behaviour than the other two HIPs in the plot.

Flame geometry

Table 3 presents observations of flame geometry obtained from video camera images. Flame height and depth were generally lower in S5 than L2G, with flame heights averaging 0.45 m and flame depth averaging 0.75 m. L2G HIP 1 showed an average flame height of 0.90 m and average flame depth of 1.30 m. L2G HIP 2 had an average flame height of 0.60 m and flame depth of 2.30 m. L2G HIP 3 showed an average flame height of 0.75 m and depth of 1.50 m. Due to the low intensity of the measurements, the values have a high level of variability as indicated by the standard deviation (s.d.) associated with each burn plot.

Rate of spread

Table 4 presents ROS values derived from infrared images of fire spread, fire arrival times and sensor locations for both burn plots. All three methods were used for plot S5. The three methods suggest overall ROS of 0.24, 0.23 and 0.26 m s^{-1} respectively. The largest s.d. occurs for the video-derived values, which in our opinion are the most subjective. The between-sensor values derived using the second method range

Fig. 4. Images of fire burning through plot S5 (*a*) and plot L2G (*b*).

Table 3. Flame properties derived from video images
FBP, fire behaviour package; ID, identifier

Plot	Camera	Flame height (m)	Flame depth (m)	FBP ID
S5	6	0.3–0.6	0.3–1.0	14
S5	8	0.3–0.6	0.3–1.0	3, 15
S5	9			18
S5	14	0.3–0.6	0.3–1.0	7, 10, 14
S5	15	0.3–0.6	1–1.5	5, 7, 10
Average		0.45	0.75	
s.d.		0.474	0.903	
L2G-HIP 1	4	0.3–1.0	1–1.5	
	12	0.3–1.0	0.3–1.5	
	14	1–1.5	1–1.5	
	18	0.3–1.0	0.3–1.5	
	19	0.3–1.0	1–1.5	
	20	1.5–1.8	1.5–3.0	
Average		0.90	1.30	
s.d.		1.044	1.46	
L2G-HIP 2	1	0.3–1.0	1.5–3.0	
	3	0.3–1.0	1.5–3.0	
	7			
	8	0.3–1.0	1.5–3.0	
	9	0.3–1.0	1.5–3.0	
Average		0.60	2.30	
s.d.		0.738	2.370	
L2G-HIP 3	5	0.3–1.0	1–1.5	
	6	0.3–1.0	1.5–3	
	13	0.3–1.0	1–1.5	
	15	0.6–1.2	1–1.5	
	16	0.6–1.2	1–1.5	
	17	0.6–1.2	1–1.5	
Average		0.75	1.50	
s.d.		0.85	1.51	

from 0.11 to 0.35 m s^{-1}. This can be seen in Fig. 5, which uses the ROS and peak intensity values to illustrate the variability of fire behaviour and intensity between sensors.

For plot L2G, only the first and last methods were used to determine ROS (e.g. ROS based on FBP flame arrival after ignition time, and ROS estimated from video images). This is due to the positioning of the FBPs in groups rather than along transects as well as the ignition pattern generated by the ignition method (Fig. 3). The agreement between the two methods is not nearly as close as that for S5. L2G HIP 1 values are 0.23 and 0.40 m s^{-1} for the two methods; HIP 2 values are 0.44 and 0.36 m s^{-1}; and HIP 3 values are 0.23 and 0.42 m s^{-1} respectively. Variability in individual observations is lowest for HIP 2.

Energy measurements

Measurements of peak heat fluxes, temperature and energy over the duration of flaming combustion at the FBP location are presented in Table 5. Fig. 6 is presented to provide context for the values. The left column of Fig. 6 presents observations from FBP7 for S5. The peak temperature was 860°C, although it was very short lived (Fig. 6*a*), lasting less than 1 s. Peak radiant, convective, and total heat fluxes were 3.6, 4.3 and 7.2 kW m^{-2}, respectively (Fig. 6*c*). Flame residence time was nominally 7 s. Average radiant, convective and total energy fluxes at the sensor faces during the flame presence were 2.1, 1.7 and 3.8 kW m^{-2}, respectively (Fig. 6*e*). The right column of Fig. 6 presents values for selected sensor FBP 22 deployed on L2G HIP 1. Based on video images, the values represent those characteristic of a head fire. As shown, the peak magnitude in air temperature was 1159°C (Fig. 6*b*). Peak heat fluxes at the sensor were 18.8 (radiant), 18.2 (convective) and 36.7 (total) kW m^{-2} (Fig. 6*d*). Average radiant, convective and total heat fluxes during the flaming phase were 11.1, 7.8 and 19.3 kW m^{-2}, respectively. Peak fire total, radiative and convective energy per unit area were 261, 143, and 118 kW m^{-2} respectively (Fig. 6*f*).

Average peak temperature (T) for all FBPs in S5 was 682°C; average peak heat fluxes (Q) were 8.6, 3.7 and 5.5 kW m^{-2} (total, radiant and convective respectively); and average flame residence time (t_{flame}) was 12.3 s. The overall averages of the mean radiant, convective and total heat fluxes during flame presence were 2.7, 2.3, and 4.9 kW m^{-2}, respectively (Table 5). Average peak temperature for all FBPs in L2G was 805°C; average peak heat fluxes were 10.1, 10.6 and 20 kW m^{-2} (radiant, convective and total, respectively); and average flame residence time was 10.0 s. The average mean heat fluxes during flame presence were 6.8 (radiant), 3.8 (convective) and 10.4 (total) kW m^{-2} (Table 5). Average fire energy values per unit area were 104, 68 and 38 kJ m^{-2}.

Average peak upward vertical flow for all FBPs during the S5 burns as the fire passed over the sensors was 4.9 m s^{-1}, average

Table 4. Fire rate of spread
FBP, fire behaviour package; ID, identifier; ROS, rate of spread

Plot	FBP ID	ROS based on FBP flame arrival time from ignition (m s^{-1})	Distance used to calculate ROS for column to left (m)	ROS based on transit time between sensors (m s^{-1})	Camera # associated with fire behaviour package[1]	ROS estimated from video images (m s^{-1})
S5	18	0.28	47	0.28	9	0.56
	15	0.24	52	0.11		
	3	0.25	67	0.27	8	0.16
	10	0.23	92	0.20	14	0.12
	14	0.21	97	0.16	6	0.21
	7	0.23	125	0.35		
	5	N/A		N/A		
	Average	0.24		0.23		0.26
	s.d.	0.02		0.09		0.20
L2G-HIP 1	22	0.32	83		4	0.24
	2	0.24	81		14	0.31
	20	0.25	86		19	0.44
	3	0.22	84		20	0.61
	14	0.22	84			
	19	0.10	62			
	17	–				
	Average	0.23				0.40
	s.d.	0.07				0.16
L2G-HIP 2	21	0.33	46		1	0.34
	6	0.46	82		3	0.25
	5	0.47	99		8	0.38
	13	0.47	101		9	0.47
	15	0.44	94			
	7	0.45	104			
	4	0.48	117			
	Average	0.44				0.36
	s.d.	0.05				0.09
L2G-HIP 3	12	0.25	46		5	0.46
	10	0.39	82		6	0.51
	16	0.16	99		13	0.38
	11	0.30	101		16	0.43
	8	0.27	94			
	18	0.16	104			
	9	0.10	117			
	Average	0.23				0.42
	s.d.	0.10				0.07

[1]The associated FBP in column 2 was used for the ROS calculation.

peak downward flow was 3.0 m s^{-1}, average peak flow in the direction of flame front spread was 8.8 m s^{-1}, and average flow in the opposite direction of fire front spread was 1.5 m s^{-1}. Average peak upward vertical flow across all FBPs distributed over the three HIPs during the L2G burns as the fire passed over the sensors was 4.9 m s^{-1}, average peak downward flow was 3.7 m s^{-1}, average peak flow in the direction of flame front spread was 7.6 m s^{-1}, and average flow in the opposite direction of fire front spread was 5.1 m s^{-1}.

Significant differences between two of the approaches used to determine ROS as well as energy and temperature measurements are presented in Table 6. Video-based ROS measurements were significant for those associated with S5, but not for plot L2G. ROS measurements based on time and distance observations were significant for all plots. Peak total heat rates were only significant for S5. Average total heat flux measurements were significant across all plots. Total fire energy estimates were only significant for plot S5. There were no significant differences in air temperature measurements reported here.

Discussion

Observations and metrics of flame size, fire ROS, and radiant and convective heating rates suggest low-intensity fire for both burns. The observations in Table 2 indicate that most FBPs in S5 were exposed to low-intensity flanking fire. This is supported in overhead infrared images. L2G seems to have burned most uniformly in the vicinity of HIP 2. Measurements made at HIP 1 and HIP 3 are characteristic of lower-intensity fire behaviour

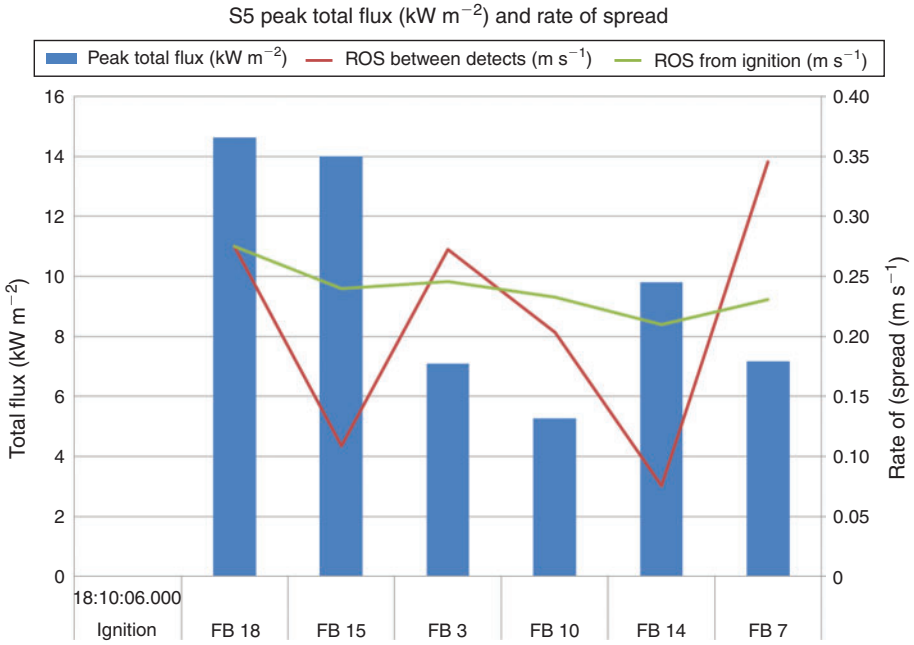

Fig. 5. Example of the variability in rate of spread (ROS) as fire moves between sensors. Blue bars represent total measured energy at sensor, red line presents rate of spread between sensors calculated from time of arrival at each sensor and distance between sensors, and green line represents overall rate of spread since fire was ignited to the sensor location.

suggesting a sporadic fire front, which is supported by the video imagery. Overall the sensor failure rate was low (nominally 4 of 28 deployments), but fire intensity in the vicinity of many of the sensors was so low as to negate use of the data, especially in unit L2F.

Table 3 data relative to S5 suggest that the use of distance between FBP and ignition line to compute fire ROS provides the lowest measurement uncertainty, but shows little of the variability of ROS indicated by other methods and exhibited by the fire. Estimates based on distance and time of spread between FBPs provide a metric of local variability in fire ROS. Estimates obtained from observation of video images show the greatest measurement uncertainty (i.e. s.d.), but the average is within 13% of the averages obtained from the other two methods.

The variability in ROS data was characterised by the ratio of the s.d. to the mean. For the values derived from ignition line to FBP sensor, the s.d.-to-value ratio was nominally 0.10; for the value derived from travel time between sensors, the ratio was nominally 0.40; for the values derived from the video images, the ratio was 0.80. For high-intensity fire, Taylor *et al.* (2004) indicate s.d.-to-value ratios below 0.06. However, Cruz *et al.* (2013) report s.d.-to-value ratios of 0.50. The data collected in this study suggest that ROS based on one or two local measurements is associated with significant uncertainty; however, averaging measurements based on four or more nearby but separate observations reduces measurement variability to within 13% of overall average ROS. However; this trend is not fully supported by the observations associated with L2G for which it appears that the greatest variability is associated with the observations from video images. For example, HIP 2 had the most observations of head fire spread, and the ROS values derived from the 'ignition-to-instrument' and 'video observation' methods agree most closely in this plot. HIPs 1 and 3 have greater variability in fire spread types and associated ROS (HIP 1 ROS derived from arrival at FBP was 0.23 m s^{-1} whereas the video-derived ROS was 0.40 m s^{-1}); the values for HIP 3 were 0.23 and 0.42 respectively. These observations imply that even in locations selected for uniform vegetation, micro-scale variations in plant spacing, type and density can significantly affect overall fire spread and intensity and are best captured by discrete sensors spaced throughout the burn plot.

Flame geometry measurements from observations of video footage have high potential for error due to the difficulty in determining length scales in a two-dimensional image. Perhaps this challenge contributed to the variability in the observations for the burns discussed here. Camera images were somewhat clouded or otherwise compromised due to deposition of soot and debris on the windows, or improper deployment. Integration of higher-quality images would perhaps reduce the variability in this measurement.

The energy and heating levels presented in Fig. 6 and Table 5 suggest that S5 burned with substantially lower intensity than L2G. However, the within-plot variability (as indicated by s.d.) suggests that S5 burned more uniformly than L2G. This is not necessarily supported by visual observations of fire images from the two burns, although it makes sense given the within-plot variability in ROS and fire spread type variability for the HIPs in L2G.

The integral of the heating curves, presented as the fire total, radiative and convective energy per unit area (*FTE*, *FRE* and *FCE* in Figs 6(*e*) and 6(*f*)) indicate that the arrival and completion of flaming combustion can be indicated by significant upturn in the derivative of the energy curve. For example,

Table 5. Energy measurements

FBP, fire behaviour package; ID, identifier; Q_R, peak radiant flux at the sensor; Q_C, peak convective heat flux at sensor; Q_T, peak measured total heat flux at sensor; E_F, flame emissive power from narrow angle sensor; T_{air}, peak kinetic air temperature; t_{flame}, flame residence time from air temperature data; $\overline{Q_R}$, average radiative heat flux over flaming period; $\overline{Q_C}$, average convective flux over the flaming period; $\overline{Q_T}$, average total heat at sensor for flaming period; *FRE*, fire radiative energy; *FCE*, fire convective energy; *FTE*, fire total energy

Plot	FBP ID	Q_R (kW m^{-2})	Q_C (kW m^{-2})	Q_T (kW m^{-2})	E_F (kW m^{-2})	T_{air} (C)	t_{flame} (s)	$\overline{Q_R}$ (kW m^{-2})	$\overline{Q_C}$ (kW m^{-2})	$\overline{Q_T}$ (kW m^{-2})	I_B^A (MW m^{-1})	*FRE* (kJ m^{-2})	*FCE* (kJ m^{-2})	*FTE* (kJ m^{-2})
S5	3	2.6	4.8	7.1	16.2	869	5	1.4	1.4	2.8		7	7	14
	35	1.1	1.3	2.2	3.8	284	–	–	–	–		–	–	–
	37	3.6	4.3	7.2	6.2	860	13	2.1	1.7	3.8		27.3	22.1	49.4
	310	3	2.9	5.3	17.7	575	20	1.9	0.8	2.7		38	16	54
	14	4.9	5	9.8	11.6	–	5[B]	3.2	2.3	5.5		16	11.5	27.5
	15	5.5	9.5	14	23.9	–	[C]	3.6	4.5	8.1		28.8	36	64.8
	18	5.2	10.9	14.6	21.8	821	23	3.9	2.8	6.7		89.7	64.4	154.1
	Average	3.7	5.5	8.6	14.5	682	12.3	2.7	2.3	4.9	0.89	33.1	27.8	60.8
	s.d.	1.6	3.4	4.5	7.6	253	7.7	1	1.3	2.2		7.9	10.1	17.1
L2G														
HIP 1	22	18.8	18.2	36.7	95.1	1159	21	11.1	7.8	19.3		143	118	261
	2	14.1	18.2	32.3	70.5	406	7	8.9	7.7	16.9		62.3	53.9	118.3
	20	7.5	5.6	12.5	13.2	644	16	4.7	1.1	5.9		75.2	17.6	94.4
	3	15.5	15.7	30.8	38.8	1280	14	9.1	4.8	14.1		127.4	67.2	197.4
	14	8.9	7.8	13.6	29.6	–	22[C]	–	–	–		–	–	–
	19	1.6	7.6	8.8	7.9	804	4	2.2	2.9	0.7		8.8	11.6	2.8
	17	0.2	0.5	0.7	13.9	915	4	–	–	–		–	–	–
	Average	9.5	10.5	19.4	38.4	868	11	7.2	4.9	11.4	1.0	79.2	53.5	125.2
	s.d.	7	6.9	13.8	32.9	324	7	3.6	2.9	7.8		25.6	20.7	55.1
HIP 2	21	3.5	10.5	12.9	15.3	755	10	2	3.1	5.2		20	31	52
	6	10.1	16.8	26.9	28.7	1106	5	6.9	8.1	15		27.6	32.4	60
	5	14.5	10.6	23.5	30.9	1125	10	9.7	4.1	13.9		97	41	139
	13	11.8	14.8	25.5	50.5	494	1	9.4	5.6	15		47	28	75
	15	9.3	13.5	22.1	34.3	857	7	6.8	7.4	14.2		47.6	51.8	99.4
	7	15.9	9.9	24	35.8	695	10[B]	11.5	4.2	15.6		115	42	156
	4	9.1	5.3	13.2	21.4	629	4	7.6	0.8	8.7		30.4	3.2	34.8
	Average	10.6	11.7	21.2	31	809	7.1	7.7	4.8	12.5	2.1	55	34	89.4
	s.d.	4.1	3.8	5.7	11.3	237	2.9	3	2.5	4		8.7	7.2	11.3
HIP 3	12	10.2	11	20	40.3	–	15	6.9	1.7	8.6		103.5	25.5	129
	10	16.3	14.1	30.2	80.9	425	6	10.2	2.5	12.8		61.2	15	76.8
	16	7.3	5.8	13.1	65	860	10	5	1.2	6.2		50	12	62
	11	9.9	7.4	16.2	35	576	17[C]	6.9	1.8	8.6		117.3	30.6	146.2
	8	15.8	14	29.8	23.8	1013	16	10.1	3.2	13.3		161.6	51.2	212.8
	18	9.2	8.9	17.7	24.2	1003	14	5.3	3	8.3		74.2	42	116.2
	9	2.7	6.1	8.6	17.4	393	5[C]	1.8	3.8	6.3		9	19	31.5
	Average	10.2	9.6	19.4	41	739	11.9	6.6	2.5	9.2	2.1	78.3	29.1	108.6
	s.d.	4.7	3.5	8.1	23.6	307	4.9	3	0.9	2.8		14.5	4.6	13.9
L2G	Mean	10.1	10.6	20	36.8	805	10	6.8	3.8	10.4		67.7	37.5	103.8
	s.d.	5.2	4.8	9.3	23.4	275	5.3	3.4	2.5	5.3		58	34.8	90.7

[A]Byram's intensity based on average ROS from flame arrival time and average consumption for each plot.
[B]Temperature did not exceed 300°C. Therefore, the residence time is computed as time above 100°C.
[C]Temperature sensor failed. Residence time is computed as time that total heat flux exceeds 5 kW m^{-2}.

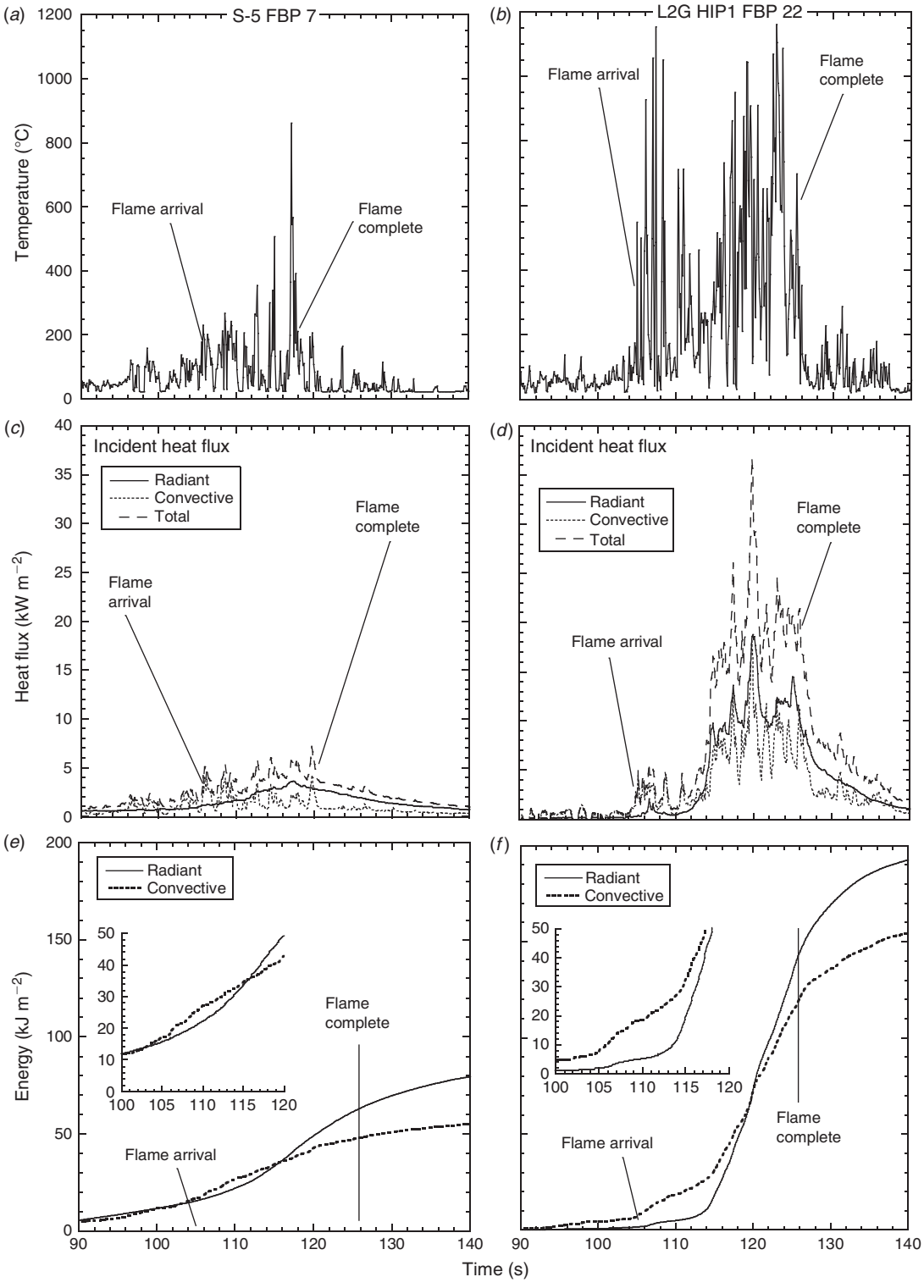

Fig. 6. Selected measurements from S5 (left column) and L2G HIP 1 (right column).

the fire arrival in Fig. 6(*f*) corresponds to the upward curvature in the *FCE* curve, whereas there is little change in the *FRE* curve. Second it seems significant that *FCE* exceeds *FRE* at the time of flame arrival. Although this trend is not consistent across all sensors it is present in a large proportion of them. It suggests that convective heating, although associated with rapid and large fluctuations in magnitude and duration of heating to cooling, is associated with the ignition of the vegetation. This observation

Table 6. Analysis of variance for selected variables
ROS, rate of spread; ID, identifier

Variable	Plot ID	Average	Variance	*P*-value	Significant difference?
ROS based on video	S5	0.263	0.041	0.341	yes
	L2G HIP 1	0.400	0.026	0.582	no
	L2G HIP 2	0.360	0.008		
	L2G HIP 3	0.445	0.003		
ROS based on time and distance from flame front to sensors	S5	0.240	0.001	<0.001	yes
	L2G HIP 1	0.225	0.005	<0.001	yes
	L2G HIP 2	0.443	0.003		
	L2G HIP 3	0.233	0.010		
Peak total heat rate, Q_t	S5	9	20	0.051	yes
	L2G HIP 1	19	190	0.925	no
	L2G HIP 2	21	33		
	L2G HIP 3	19	66		
Average total heat rate, Q_t ave	S5	5	5	0.033	yes
	L2G HIP 1	11	61	0.452	yes
	L2G HIP 2	13	16		
	L2G HIP 3	9	8		
Total fire energy, *FTE*	S5	61	2439	0.275	yes
	L2G HIP 1	135	9793	0.512	no
	L2G HIP 2	88	2072		
	L2G HIP 3	111	3641		
Peak air temperature, T_{air}	S5	682	63 957	0.648	no
	L2G HIP 1	868	104 870	0.631	no
	L2G HIP 2	809	56 318		
	L2G HIP 3	712	79 962		

suggests that though radiative heating contributes to the pyrolysis process, convective heating is the major driver of ignition (as would be expected for piloted ignition), and the convective events though short-term are sufficient to lead to ignition of the irradiated vegetation. Others have drawn similar conclusions from laboratory studies (Frankman 2009; Anderson *et al.* 2010; Finney *et al.* 2010; Frankman *et al.* 2010; McAllister *et al.* 2012).

The energy release rates presented here are substantially lower than values reported by others (Clements *et al.* 2007; Frankman *et al.* 2013*a*). Total fuel consumption for plot S5 was nominally 0.22 kg m^{-2} and for L2G HIP 1 was 0.25 kg m^{-2}. Fuel loadings reported by Frankman *et al.* (2013*a*, *b*) in similar fuel types were 0.3 kg m^{-2} with peak radiant fluxes recorded at 75 kW m^{-2} for frontal fire spread and 24 kW m^{-2} for lateral fire spread. Clements *et al.* (2007) reports measurements from a fire burned in similar fuel type but with much higher loading (1.1 kg m^{-2}) (although no direct measurements of energy release from oblique-oriented sensors were recorded); however, the vertical and horizontal air flow measurements fall generally in line with magnitudes recorded in S5 and L2G plots. We postulate that the differences in heating rates between the burns reported here and those reported by Frankman *et al.* (2013*a*) are due to the significantly greater woody fuels and litter load in the Frankman *et al.* (2013*a*) burns. Although total fuel loading was not significantly different, the litter load in the Frankman burns was 2–4 times greater and the woody fuels loading was 10–100 times greater.

The results of the ANOVA for ROS based on video imagery measurements suggest that there is a significant difference in this method between plot S5 and Plot L2G, but no significant difference between HIPs on L2G (Table 6). When ROS is based on time and distance between ignition and the sensors, there was a significant difference between S5 and L2G, and between the individual HIP plots in L2G. When evaluating peak total heat incident on the sensor there was a significant difference between the S5 plot and L2G data, but no significant difference between the HIP plots in L2G. When considering average incident total heat, there were significant differences between S5 and L2G and between the HIPs in L2G. Fire total energy showed a significant difference between S5 and L2G but not within the HIPs in L2G. No significant differences were found for air temperature. These data imply that video-based ROS values include greater random variation than those based on calculated times and distances between the fire and sensors. When characterising fire intensity in terms of heating of sensors, average values show less random variation than peak or instantaneous values. Therefore, ROS (derived from time and distances) and heating rates (based on time-averaged values) suggest significant differences between all burn plots.

Conclusions

The measurement of energy and mass transport in reacting systems is at best tenuous. In the context of wildland fire it is even more difficult and is associated with increased measurement

uncertainty due to the fluctuating nature of the wildland fire environment. The data described here are part of the larger RxCADRE dataset, and build on what has historically been a limited dataset of similar measurements. Although the data presented in this work embody the low end of the spectrum of fire intensity, and are not as visually stimulating as what would be expected from heavier fuels (e.g. forests) that produce larger flames, they do represent an important first step in the building of a comprehensive dataset and will support future development of fire behaviour, effects and emissions models. Additionally, these data are integral to a better understanding of the contributions of radiative and convective heating to energy transport.

The measurements reported here are a first look at a subset of the RxCADRE dataset, and suggest that quantification of fire intensity is improved when the number of sensors deployed on the ground is increased. Generally the data suggest that fires in short grass of relatively low stem density can be characterised by residence times of nominally 10–12 s. Air temperatures average 830°C with peak temperatures reaching nearly 1300°C. Heating values can reach 36 kW m^{-2}; however, the average total heating is ~20 kW m^{-2} with radiant and convective heating reaching 10 kW m^{-2}. Maximum average upward air flow at the sensor reached nearly 5.4 m s^{-1}, downward flow reached 4 m s^{-1}, maximum horizontal flow in the direction of flame spread reached 8.9 m s^{-1}, and flow in the opposite direction reached 3.3 m s^{-1}. Perhaps one of the most significant findings from this effort is that the magnitude of convective heating is in the order of radiant heating, and is associated with ignition of the vegetation. This suggests that both heating modes must be measured to adequately quantify the heating environment around fires in this vegetation type. Further analyses of all the data collected in this effort will likely provide additional information in this regard. As in any field campaign, several aspects regarding sensor setup and experimental methods could be improved, including distance and height metrics in the camera field of view, measurement and recording of the height of sensors relative to vegetation height, overhead infrared imagery in developing continuous fire ROS information, additional measurements and analysis of flame temperature data from very fine wire thermocouples, and additional measurements at high sampling rates to further characterise the temporal properties of energy release from flames.

Acknowledgements

The financial support provided by the Joint Fire Science Program (Project #11–2–1–11) was crucial to this effort. The integrative and collaborative involvement of the many groups involved in the effort facilitated the deployment and collection of a large number of fire behaviour packages. The leadership provided by R. Ottmar facilitated the efficient and productive execution of the project. Finally, none of this work would have been possible without the collaborative support of the administration and fire management organisation at Eglin Air Force Base.

References

Albini FA (1985) A model for fire spread in wildland fuels by radiation. *Combustion Science and Technology* **42**, 229–258. doi:10.1080/00102208508960381

Albini FA (1986) Wildland fire spread by radiation – a model including fuel cooling by natural convection. *Combustion Science and Technology* **45**, 101–113. doi:10.1080/00102208608923844

Albini FA (1996) Iterative solution of the radiation transport equations governing spread of fire in wildland fuel. *Combustion, Explosion, and Shock Waves* **32**, 534–543. doi:10.1007/BF01998575

Anderson HE (1969) Heat transfer and fire spread. USDA Forest Service, Intermountain Forest and Range Experiment Station, Research Paper INT-69. (Ogden, UT)

Anderson WR, Catchpole EA, Butler BW (2010) Convective heat transfer in fire spread through fine fuel beds. *International Journal of Wildland Fire* **19**, 284–298. doi:10.1071/WF09021

Bryant R, Womeldorf C, Johnsson E, Ohlemiller T (2003) Radiative heat flux measurement uncertainty. *Fire and Materials* **27**, 209–222. doi:10.1002/FAM.822

Butler BW (1993) Experimental measurements of radiant heat fluxes from simulated wildfire flames. In '12th International Conference of Fire and Forest Meteorology', 26–28 October 1993. Jekyll Island, Georgia. (Eds JM Saveland, J Cohen) Volume 1 pp. 104–111. (Society of American Foresters: Bethesda, MD)

Butler BW (2003) Field measurements of radiant energy transfer in full scale wind driven crown fires. In 'Proceedings of the 6th ASME-JSME Thermal Engineering Joint Conference, AJTEC 2003', 16–30 March 2003, Kohala Coast, Hawaii Island, Hawaii. (Japan Society of Mechanical Engineers: Tokyo)

Butler BW (2014) Wildland firefighter safety zones: a review of past science and summary of future needs. *International Journal of Wildland Fire* **23**, 295–308. doi:10.1071/WF13021

Butler BW, Cohen JD (1998) Firefighter safety zones: a theoretical model based on radiative heating. *International Journal of Wildland Fire* **8**, 73–77. doi:10.1071/WF9980073

Butler BW, Jimenez D (2009) *In situ* measurements of fire behavior. In '4th International Fire Ecology & Management Congress: Fire as a Global Process', 30 November–4 December 2009, Savannah, GA. (Ed. S Rideout-Hanzak) (Association for Fire Ecology: Eugene, OR)

Butler BW, Cohen J, Latham DJ, Schuette RD, Sopko P, Shannon KS, Jimenez D, Bradshaw LS (2004) Measurements of radiant emissive power and temperatures in crown fires. *Canadian Journal of Forest Research* **34**, 1577–1587. doi:10.1139/X04-060

Clements CB, Perna R, Jang M, Lee D, Patel M, Street S, Zhong S, Goodrick S, Li J, Potter BE (2007) Observing the dynamics of wildland grass fires: FireFlux – a field validation experiment. *Bulletin of the American Meteorological Society* **88**, 1369–1382. doi:10.1175/BAMS-88-9-1369

Cruz MG, McCaw WL, Anderson WR, Gould JS (2013) Fire behaviour modelling in semi-arid mallee-heath shrublands of southern Australia. *Environmental Modelling & Software* **40**, 21–34. doi:10.1016/J.ENVSOFT.2012.07.003

Finney MA, Cohen JD, Grenfel IC, Yedinak KM (2010) An examination of fire spread thresholds in discontinuous fuel beds. *International Journal of Wildland Fire* **19**, 163–170. doi:10.1071/WF07177

Frankman D (2009) Radiation and convection heat transfer in wildland fire environments. PhD Thesis, Brigham Young University, Provo, UT

Frankman D, Webb BW, Butler BW (2010) Time-resolved radiation and convection heat transfer in combusting discontinuous fuel beds. *Combustion Science and Technology* **182**, 1391–1412. doi:10.1080/00102202.2010.486388

Frankman D, Webb BW, Butler BW, Jimenez D, Forthofer JM, Sopko P, Shannon KS, Hiers JK, Ottmar RD (2013*a*) Measurements of convective and radiative heating in wildland fires. *International Journal of Wildland Fire* **22**, 157–167. doi:10.1071/WF11097

Frankman D, Webb BW, Butler BW, Jimenez D, Harrington M (2013*b*) The effect of sampling rate on interpretation of the temporal characteristics of radiative and convective heating in wildland flames. *International Journal of Wildland Fire* **22**, 168–173. doi:10.1071/WF12034

Freeborn PH, Wooster MJ, Hao WM, Ryan CA, Nordgren BL, Baker SP, Ichoku C (2008) Relationships between energy release, fuel mass loss,

and trace gas and aerosol emissions during laboratory biomass fires. *Journal of Geophysical Research* **113**, D01301. doi:10.1029/2007JD008679

Jimenez D, Forthofer JM, Reardon JJ, Butler BW (2007) Fire behavior sensor package remote trigger design. In 'The Fire Environment – Innovations, Management, and Policy', 26–30 March 2007, Destin, FL. (Eds Butler BW, Cook W) USDA Forest Service, Rocky Mountain Research Station, Proceedings RMRS-P-46CD, pp. 499–505. (Fort Collins, CO)

Jimenez D, Butler BW, Teske C, O'Brien J, Loudermilk EL, Hornsy B, Clements C (2014) Wind flow characterization associated with fire behavior measurements. In 'Advances in forest fire research'. (Ed. DX Viegas) pp. 500–508. (Imprensa da Universidade de Coimbra: Associação para o Desenvolvimento da Aerodinâmica, Industrial Centro de Estudos sobre Incêndios, Florestais Coimbra, Portugal)

McAllister S, Grenfell I, Hadlow A, Jolly W, Finney M, Cohen J (2012) Piloted ignition of live forest fuels. *Fire Safety Journal* **51**, 133–142. doi:10.1016/J.FIRESAF.2012.04.001

McCaffrey BJ, Heskestad G (1976) A robust bidirectional low-velocity probe for flame and fire application. *Combustion and Flame* **26**, 125–127. doi:10.1016/0010-2180(76)90062-6

Morandini F, Silvani X (2010) Experimental investigation of the physical mechanisms governing the spread of wildfires. *International Journal of Wildland Fire* **19**, 570–582. doi:10.1071/WF08113

Omega Engineering Inc (n.d.) Thermocouple response time. Available at http://www.omega.com/temperature/Z/ThermocopuleResponseTime.html [Verified 11 June 2014]

O'Brien JJ, Loudermilk EL, Hornsby B, Hudak AT, Bright BC, Dickinson MB, Hiers JK, Teske C, Ottmar RD (2015) High-resolution infrared thermography for capturing wildland fire behaviour – RxCADRE 2012. *International Journal of Wildland Fire* **25**, 62–75. doi:10.1071/WF14165

Ottmar R, Hiers JK, Butler BW, Clements CB, Dickinson MB, Hudak AT, O'Brien JJ, Potter BE, Rowell EM, Strand TM, Zajkowski TJ (2015) Measurements, datasets and preliminary results from the RxCADRE project – 2008, 2011 and 2012. *International Journal of Wildland Fire* **25**, 1–9. doi:10.1071/WF14161

Parent G, Acem Z, Lechene S, Boulet P (2010) Measurement of infrared radiation emitted by the flame of a vegetation fire. *International Journal of Thermal Sciences* **49**, 555–562. doi:10.1016/J.IJTHERMALSCI.2009.08.006

Pitts WM, Murthy AV, de Ris J, Filtz J, Nygard K, Smith D, Wetterlund I (2006) Round robin study of total heat flux gauge calibration at fire laboratories. *Fire Safety Journal* **41**, 459–475. doi:10.1016/J.FIRESAF.2006.04.004

Sacadura JF (2005) Radiative heat transfer in fire safety science. *Journal of Quantitative Spectroscopy & Radiative Transfer* **93**, 5–24. doi:10.1016/J.JQSRT.2004.08.011

Taylor SW, Wotton BM, Alexander ME, Dalrymple GN (2004) Variation in wind and crown fire behaviour in a northern jack pine black spruce forest. *Canadian Journal of Forest Research* **34**, 1561–1576. doi:10.1139/X04-116

Urbanski SP, Hao WM, Baker S (2008) Chemical composition of wildland fire emissions. In 'Developments in Environmental Science Vol. 8'. (Eds A Bytnerowicz, MJ Arbaugh, AR Riebau, C Andersen) pp. 79–107. (Elsevier: New York, NY). doi:10.1016/S1474-8177(08)00004-1

Viskanta R (2008) Overview of some radiative transfer issues in simulation of unwanted fires. *International Journal of Thermal Sciences* **47**, 1563–1570. doi:10.1016/J.IJTHERMALSCI.2008.01.008

Wooster MJ, Roberts G, Perry GLW, Kaufman YJ (2005) Retrieval of biomass combustion rates and totals from fire radiative power observations: FRP derivation and calibration relationships between biomass consumption and fire radiative energy release. *Journal of Geophysical Research* **110**, D24311. doi:10.1029/2005JD006318

Yedinak KM, Forthofer JM, Cohen JD, Finney MA (2006) Analysis of the profile of an open flame from a vertical fuel source. *Forest Ecology and Management* **234**, S89. doi:10.1016/J.FORECO.2006.08.125

Yedinak KM, Cohen JD, Forthofer JM, Finney MA (2010) An examination of flame shape related to convection heat transfer in deep-fuel beds. *International Journal of Wildland Fire* **19**, 171–178. doi:10.1071/WF07143